

Fast Multi-Stack Slice-to-Volume Reconstruction via Multi-Scale Unrolled Optimization

Margherita Firenze
MIT
mfirenze@mit.edu

Hyuk Jin Yun
Harvard Medical School
hyun@cmh.edu

P. Ellen Grant
Harvard Medical School
ellen.grant@childrens.harvard.edu

Sean I. Young
Harvard Medical School
siyoung@mit.edu

Elfar Adalsteinsson
MIT
elfar@mit.edu

Clinton J. Wang
MIT
clintonw@csail.mit.edu

Kiho Im
Harvard Medical School
kiho.im@childrens.harvard.edu

Polina Golland
MIT
polina@csail.mit.edu

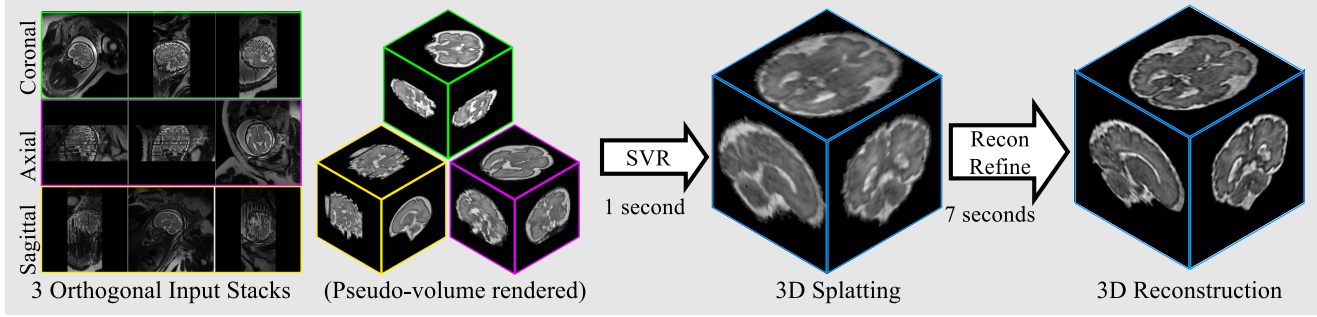


Figure 1: Fast Multi-Stack Slice-to-Volume Reconstruction. Our proposed multi-stack SVR framework takes as input three motion-corrupted stacks of 2D slices and reconstructs a volume (1 second). Super-resolution is performed With optional optimization (7 seconds).

Abstract

Fully convolutional networks have become the backbone of modern medical imaging due to their ability to learn multi-scale representations and perform end-to-end inference. Yet their potential for slice-to-volume reconstruction (SVR), the task of jointly estimating 3D anatomy and slice poses from misaligned 2D acquisitions, remains underexplored. We introduce a fast convolutional framework that fuses multiple orthogonal 2D slice stacks to recover coherent 3D structure and refines slice alignment through lightweight model-based optimization. Applied to fetal brain MRI, our approach reconstructs high-quality 3D volumes in under 10s, with ~ 1 s slice registration and accuracy on par with state-of-the-art iterative SVR pipelines, offering more than 40 \times speedup. The framework uses non-rigid displacement fields to represent transformations, generalizing to other SVR problems like fetal body and placental MRI. Additionally,

the fast inference time paves the way for real-time, scanner-side volumetric feedback during MRI acquisition.

1. Introduction

Fetal brain magnetic resonance imaging (MRI) is an important tool for investigating abnormal ultrasound findings and expanding our understanding of fetal brain development [1, 9, 15]. To alleviate the effects of fetal motion, fast 3D MRI sequences are used, which limit motion artifacts in the acquired 2D images [18]. A “cool-off” period is required due to safety limits on energy deposition between consecutive slice acquisitions [13] and during these times the fetus often moves considerably, causing the slices to be misaligned. An example of this can be seen in Fig. 1, where the coronal and sagittal views both have severe motion that make their orthogonal views look incoherent.

Images are acquired in series, called stacks, and ideally only three stacks are needed for the three standard views of the brain (sagittal, axial, and coronal). Due to motion, stacks may contain oblique (out of plane) slices. In these cases, the stack is reacquired, resulting in as many as 20 stacks and leading to long, uncomfortable scan times and thousands of images for radiologists to sift through.

These problems can be overcome by slice-to-volume reconstruction (SVR) methods, which produce high-resolution visualizations of the brain from a limited number of stacks. SVR methods align the acquired slices in 3D and super-resolve the volume [4, 7, 14, 21, 28, 29]. SVR is widely used in research for volumetric analysis. However, long runtime limits scanner-side uses and clinical adoption, as radiologists perform assessment shortly after acquisition, making time-consuming SVR methods disrupt the standard workflow. Fast SVR has the potential to improve radiological assessment by providing a coherent volume in time for radiological assessment, and to vastly accelerate and improve fetal imaging by guiding decision-making during acquisitions, i.e., when to stop acquiring new data because the brain coverage is complete and which orientation to prescribe for the next stack. Our main contributions are:

- We propose a fully convolutional neural network that registers multiple stacks of slices in under one second, and refines poses and produces reconstructions of high quality in under 10 seconds.
- We integrate the neural network with model-based reconstruction using data consistency with acquired slices.
- We evaluate the proposed method on simulated and real clinical data, demonstrating state of the art reconstruction accuracy and speed.

Notably, our framework is not constrained to rigid motion models and only requires a small training set, which paves the way for other MRI applications such as placental (deformable motion) and fetal body (poly-rigid) SVR.

2. Related Work

SVR is complicated by the fact that only 2D slices are available, unlike classic 2D-to-3D registration problems where 2D and 3D images are given. Therefore, SVR can be thought of as two problems that have to be solved jointly: volume reconstruction, i.e., recovering a high-resolution 3D volume from aligned slices, and slice registration, i.e., aligning 2D slices into a common coordinate system. These steps are intertwined, as more accurate volumes lead to more accurate slice poses and vice versa. Early optimization methods updated the volume and slice poses in an alternating fashion. Later research sought to use deep learning to solve the registration task of SVR, optimize both registration and reconstruction with a neural network, and solve registration in one pass using an unrolled deep learning approach.

Learning-free Optimization. Early methods framed SVR as an optimization problem, with solutions that alternated between reconstructing a 3D volume and estimating slice poses [5–7, 11, 12, 14, 21, 23]. The SVRTK toolkit [14] is a widely used package that improves this approach by using robust statistics to remove outlier slices for better reconstructions.

In SVRTK the volume is initialized using a designated reference stack. To initialize the slice poses, stacks are registered to the reference stack in bulk, setting poses of all slices in the stack. Following this step, the volume reconstruction is achieved by minimizing a model-based loss. The optimization encourages the simulated slices, the slices predicted based on the volume and slice pose estimates, to match the input slices. Then, the poses are updated by registering the input slices to the latest volume estimate. These steps are repeated 5-7 times. The optimization can fail to converge when large motion is present [24] or a reference stack is not adequately chosen. Further, the method is time consuming taking around 5 minutes using a multi-threaded CPU implementation to reconstruct a volume from 3 slice stacks. Finally, SVRTK predicts poses relative to a designated template stack, with no guarantees of the final reconstruction being in a canonical orientation that can be readily interpreted by radiologists, resulting in oblique reconstructions.

Deep Learning Registration for SVR. Deep learning promised to make SVR more robust to large motion and to reconstruct the volume in the canonical orientation. Early deep learning approaches for SVR used CNN architectures trained on synthetic data to directly regress slice poses, either as explicit rotation and translation parameters [22] or as anchor-point representations [10, 17]. Transformer architecture has been shown effective for coupled registration of all slices in the stack by capturing their pose similarities [28]. While these methods were fast, none were accurate enough to outperform traditional optimization-based approaches, but rather served as an initialization step to lead to faster convergence using optimization methods. State-space architectures followed by an MLP to predict slice poses have been shown to achieve improved registration accuracy [27].

In many deep learning SVR methods, once slice poses are estimated, the latent volume is reconstructed using traditional model-based optimization [14]. Alternatively, the model-based reconstruction alternates with registration as in classical methods [28]. Other methods replace this step with learned reconstruction networks, employing supervised interpolation to perform super-resolution and inpainting [27, 30]. While supervised inpainting methods produce high-quality details, they are not guaranteed to produce a final reconstruction that is consistent with the input slices. This has the potential to smooth over potential

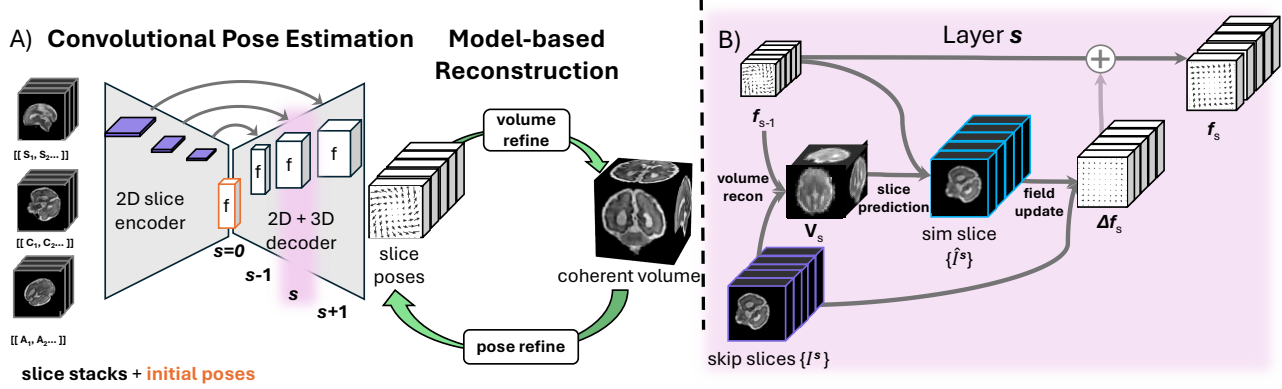


Figure 2: Method Overview. (A) SVR pipeline combines convolutional pose estimation with model-based reconstruction. (B) Iterative 2D+3D blocks refine slice pose estimates at resolution s through simulated slice generation and flow field updates.

pathology and favor reconstructing “average” brains.

We use the model-based reconstruction approach in our method as it is faster than INR based reconstructions and ensures consistency with the acquired data. Supervised inpainting methods are not guaranteed to produce a final reconstruction that is consistent with the input slices. This has the potential to smooth over potential anomalies and favor reconstructing “average” brains [30].

Fully Neural SVR. More recently, implicit neural representations (INR) have been used to perform registration and reconstruction [4, 26, 29]. The INR optimizes a multi-layer perceptron (MLP) during inference. The INR learns a continuous representation of the volume and adapts slice poses as well as pixel and slice weights to remove outliers and bias fields effectively. The NeSVoR package [29], which first proposed this approach, is considered state of the art for its ability to resolve fine details and produce robust results. Since the network is optimized at inference time, the method requires long runtimes, around 4-5 minutes, and specialized GPU infrastructure. The poses are initialized using a fast deep-learning registration [28]. Similar to the classic methods, the optimization fails to converge when the initial poses are inaccurate. Further, in the final query of the INR to produce the volume, discretization artifacts can occur from sampling the continuous network parameterization.

Alternatively, optimizing two MLPs at inference time has been proposed. The first MLP performs registration and the second MLP provides volume reconstruction similar to the INR methods above [4, 26]. Additionally, meta learning [4] has been shown to reduce the convergence time by initializing the weights using a small set of examples. Despite these advancements the fastest implementation still requires more than a minute and specialized GPU infrastructure.

Deep Learning SVR via Multi-scale Feed-forward Networks. One possible reason for the success of the deep

learning methods in 2 is that they repeat the classical optimization steps thousands of times and parametrize the problem with millions of parameters. This is in contrast to deep registration networks which are much faster but predict poses directly from slices without explicitly evoking the forward model that couples the volume, the slice poses, and the acquired slices. In order to combine the performance gains of parameterized optimization approaches and the speed of registration approaches, a possible solution is to unroll the optimization steps across different layers of a network. Specifically SVR is posed as a 2D-to-3D registration task between input slices and an unknown 3D volume. In the network the poses are refined at different resolutions in successive layers of the network. This is done using a U-net architecture [20] which is designed multi-scale feed forward. Once trained, this network produces slice pose estimates through a single feed-forward pass at inference time, requiring less than a second [30]. Then to perform super-resolution reconstruction inpainting is used [30]. Our method expands on this work and integrates model-based reconstruction following registration.

3. Preliminaries

Formally, SVR is an inverse problem where we seek to reconstruct an underlying volume V that is consistent with the acquired slices. The forward imaging model predicts slice I_n from an underlying volume V ,

$$I_n = M(F_n^{-1})V \quad (1)$$

where $F_n \in E(3)$ is a rigid transformation that defines the plane of imaging of slice I_n and function $M(\cdot)$ transforms the 3D discretized point-spread function (PSF) by the transformation that is its input. The PSF is determined by the image acquisition parameters and can be approximated as a Gaussian [11, 21]. M produces a sparse, non-square matrix

mapping voxel coordinates in the volume to slice coordinates.

Both V and $\{F_n\}$ are unknown. Classical SVR methods use coordinate descent by alternating the estimation of V (i.e., reconstruction) and $\{F_n\}$ (i.e., registration).

The volume is initialized using the original slice poses of the acquired stacks, where each slice is spread over a 3D area given by the PSF weights and normalized by the total amount of slice contributions to a voxel, i.e.,

$$V_{\text{init}}(x) = \frac{\left[\sum_n M(F_n)^T I_n \right](x)}{\left[\sum_n M(F_n)^T \right](x)}. \quad (2)$$

This step produces blurry volumes that can be further refined by minimizing a data consistency loss. Specifically, “simulated slices” are generated from the estimated volume V the current slice poses $\{F_n\}$ and the forward model (1), and compared to the acquired slices $\{I_n\}$. This is also known as model-based optimization. Formally, the reconstruction step updates V while keeping the poses $\{F_n\}$:

$$\hat{V} = \underset{V}{\operatorname{argmin}} \sum_n \|I_n - M(F_n)V\|^2. \quad (3)$$

During registration, the acquired slices are registered to the fixed volume V to update their poses $\{F_n\}$ constant:

$$\hat{F}_n = \underset{F_n}{\operatorname{argmin}} \|I_n - M(F_n)V\|^2 \quad (4)$$

This alternating scheme separates pose and volume optimization, with each step requiring computationally expensive updates and many iterations to converge to a solution.

4. Method

We implement a reconstruction and slicing formulation that makes implementation highly parallelizable by using the first order approximations for the forward model and volume reconstruction. To generalize our approach we employ non-rigid displacements instead of rigid transforms.

We replace the discrete PSF matrix M_n with identity \mathbb{I} , modeling slices as unit thin. As we explain later in this section, this is a reasonable simplification for low-resolution layers in our network. Motion is modeled as a non-rigid displacement field $f : \mathbb{R}^2 \rightarrow \mathbb{R}^3$ mapping 2D pixel coordinates $p = (p_x, p_y)$ to 3D displacements. We uplift to 3D via p^\uparrow by placing slices on $z = 0$ plane by appending a 0 to each vector, i.e. $(p_x, p_y)^\uparrow = (p_x, p_y, 0)$. The initial volume reconstruction (2) becomes

$$V_{\text{init}}(x) = \frac{\left[\sum_n \sum_p \mathcal{V}(p^\uparrow + f_n(p), I_n(p)) \right](x)}{\left[\sum_n \sum_p \mathcal{V}(p^\uparrow + f_n(p), [I_n > 0]) \right](x)} \quad (5)$$

where $\mathcal{V}(x, I)$ denotes the volume pushing operation that places the intensity given by I at the voxel coordinates x and distributes the intensity using trilinear interpolation when the 3D coordinate location does not coincide with a discrete grid point. Finally, since multiple slices may contribute to one 3D voxel location, the intensity is normalized by the total weight of contributions. This approximation is used for slice estimation and is not refined using (3) as in classical methods.

To refine the pose estimates, we first construct the simulated slices using the current pose estimates, similar to (4), except without the use of M :

$$\hat{I}_n(p) = \mathcal{V}^*(p^\uparrow + f_n(p), V) \quad (6)$$

where $\mathcal{V}^*(x, v)$ denotes the volume sampling operation that samples the intensity at the coordinate x and uses trilinear interpolation when the 3D coordinate location does not coincide with a discrete point on the grid.

Then, we employ a learned convolutional operator, Δf which refines the displacement by comparing the simulated and input slices

$$f_n^s = f_n^{s-1} + \Delta f^s(\hat{I}_n, I'_n), \quad (7)$$

where s is the index of the layer. With these two operations defined we can implement the volume estimation and pose refinement steps many times as illustrated in Fig. 2. To implement a multi-resolution strategy, we repeat these steps at increasing resolutions, starting with slices sampled at low resolutions and ending with high-resolution slices, using a slice parametrization that accounts for orthogonal slices.

Slice pose parametrization. We initialize slice poses to their prescribed positions, as given by the stack direction and slice order, and have the network refine them through iterative updates with increasing resolution. We parametrize the slice depth using a translation matrix T_n and 3D orientation (sagittal, axial, coronal) with a 4x4 matrix R_n that corresponds to either a sagittal, axial, or coronal orientation. Then to adjust to different resolutions of the slices, we use C_s and C_s^{-1} which are translation matrices that center and de-center the coordinates to rotate about the center of the slice at resolution s . Finally, S_s scales the pixel coordinates to match the volume resolution. Note that T_n encodes the slice index in the stack and is different for each slice in the stack; R_n is shared by all slices in the same stack; C_s and S_s depend on the resolution of layer s in the network. All together this transformation can be used to formulate the displacement field that places a slice in its prescribed position at different scales s :

$$f_n^s = (C_s R_n C_s^{-1} S_s^{-1} T_n - \mathbb{I})p \quad (8)$$

where p^\uparrow denotes homogeneous 3D coordinates, for the slice placed at $z=0$. This approach models each slice sepa-

rately, enabling the framework to work with variable slice and stack numbers.

Finally, to train the network we use a multi-layer L_2 loss on the residual displacement:

$$\mathcal{L}(f_{\text{GT}}, f) = \sum_n \left\| f_{\text{GT},n} - \frac{1}{5} \sum_{s=0}^4 f_n^{s\uparrow} \right\|_2^2 \quad (9)$$

Once the network predicts the slice poses, we super-resolve the volume using a model-based approach as in (3) and also perform the pose update steps and refine the poses.

High-resolution slice and volume estimation. At low resolutions modeling slices as unit thin is viable since the in-plane sampling ratio substantially exceeds the slice thickness. However, approximating slices as unit thickness introduces rendering artifacts at full resolution due to the mismatch between the in-plane and thickness dimensions. To mitigate coverage gaps at full resolution, we project the displacement field using the method of Arun et al. [2] at the final layer, then apply a boxcar PSF to distribute slice values across their thickness.

4.1. Implementation

Network Architecture. We build a custom U-net with a 2D encoder and a 2D + 3D decoder. The encoder constructs multi-resolution slice features $\{I_n^s\}$. The decoder repeats a 2D to 3D block five times while doubling the resolution at each layer, to emulate the classical SVR steps, as shown in Panel B of Fig. 2 and 5–7.

We construct a feature volume $V^s \in \mathbb{R}^{d \times d_s \times d_s \times d_s}$ at each resolution using ((5)). V^s is a four dimensional tensor, constructed from the slice features $\{I_n^s\}$ from the skip connection of layer s and the previous displacement fields f_n^{s-1} . Here $d = [8, 16, 32, 64, 128]$ and $d_s = [1024, 512, 256, 128, 64]$.

To refine the displacement fields, we sample the volume to create simulated slices $\{\hat{I}_n^s\}$ and compute their correlation with the skip connection features $\{I_n^s\}$ to estimate a displacement residual Δf^s that is added to the previous displacement estimate f_{s-1} as in (7).

We simplify the architecture compared to previously proposed solution [30] to make each layer’s predicted volume and slices independent from the previous layer and depend only on the previous displacement estimates and skip connections.

Model-based reconstruction. The slice pose estimates are used to initialize a model-based optimization that iteratively refines both the 3D volume and slice poses to ensure consistency with the acquired slices in (3) [14]. We employ a GPU-accelerated implementation of this model-based reconstruction [28].

Training. We generate slice stacks from standard orthogonal imaging planes (sagittal, axial, and coronal), each perturbed by a bulk in-plane rotation uniformly sampled in the range $[-12^\circ, 12^\circ]$ to simulate imperfect plane selection. Starting from this initialization, we apply between 1 and 100 smooth motion perturbations per stack, generated by interpolating randomly sampled rigid transformations using cubic B-splines. This procedure captures both gradual motion patterns and abrupt movements. Rotational perturbations are drawn from a zero-mean normal distribution with a standard deviation of 20° ; translations are uniformly sampled within $[-6.1, 6.1]$ mm. We further apply Gaussian noise, slice-wise bias field augmentation, and gamma intensity perturbations to make the network robust to imaging artifacts. We train the network on a NVIDIA H200 GPU for 250k steps and pick the last model. We use ADAM with an initial learning rate of 10^{-4} and poly scheduling.

5. Experimental Results

Table 1: Clinical Evaluation. Quantitative assessment of reconstruction quality across 9 clinical subjects. We compute similarity measures (SSIM, NCC, and PSNR) between the simulated slices and input slices across methods. Running times listed (last row).

Method	Slice SSIM (\uparrow)	NCC (\uparrow)	PSNR (\uparrow)	
SVoRT	0.971 \pm 0.007	0.14 \pm 0.01	37.5 \pm 1.4	
+ NeSVoR	0.959 ± 0.007	0.13 ± 0.01	35.7 ± 1.3	
cSVR	0.952 ± 0.013	0.12 ± 0.01	35.4 ± 2.0	
+ Refine	0.966 ± 0.005	0.13 ± 0.01	37.0 ± 1.2	
+ NeSVoR	0.959 ± 0.006	0.13 ± 0.01	35.3 ± 1.2	
SVoRT	+ NeSVoR	cSVR	+ Refine	+ NeSVoR
10s	257s	3s	7s	251s

Data. We train and evaluate our model using FeTA [16], a public dataset of high-quality T2-weighted coherent volumes reconstructed using existing methods in 120 subjects (gestational age (GA) 20–35 weeks, voxel size 0.8 mm^3), and 18 volumes (GA 21–38 weeks, voxel size 0.8 mm^3) from the CRL atlas [8]. We train the network on 108 subjects and 18 atlases.

We evaluate our method on 12 held-out FeTA subjects and 9 patients from [withheld for anonymity] (GA 25 – 35 weeks, pixel size 1.3 – 1.4mm, slice thickness 3mm). We choose three stacks (sagittal, coronal, and axial) for each subject and segment the intracranial content using a publicly available method [19].

Baseline methods. We evaluate the accuracy of the pose estimates produced by our neural network when coupled with three variants of volume reconstruction: (1) cSVR keeps the slice poses estimated by the neural network and uses data consistency to reconstruct the volume; (2) cSVR+Refine

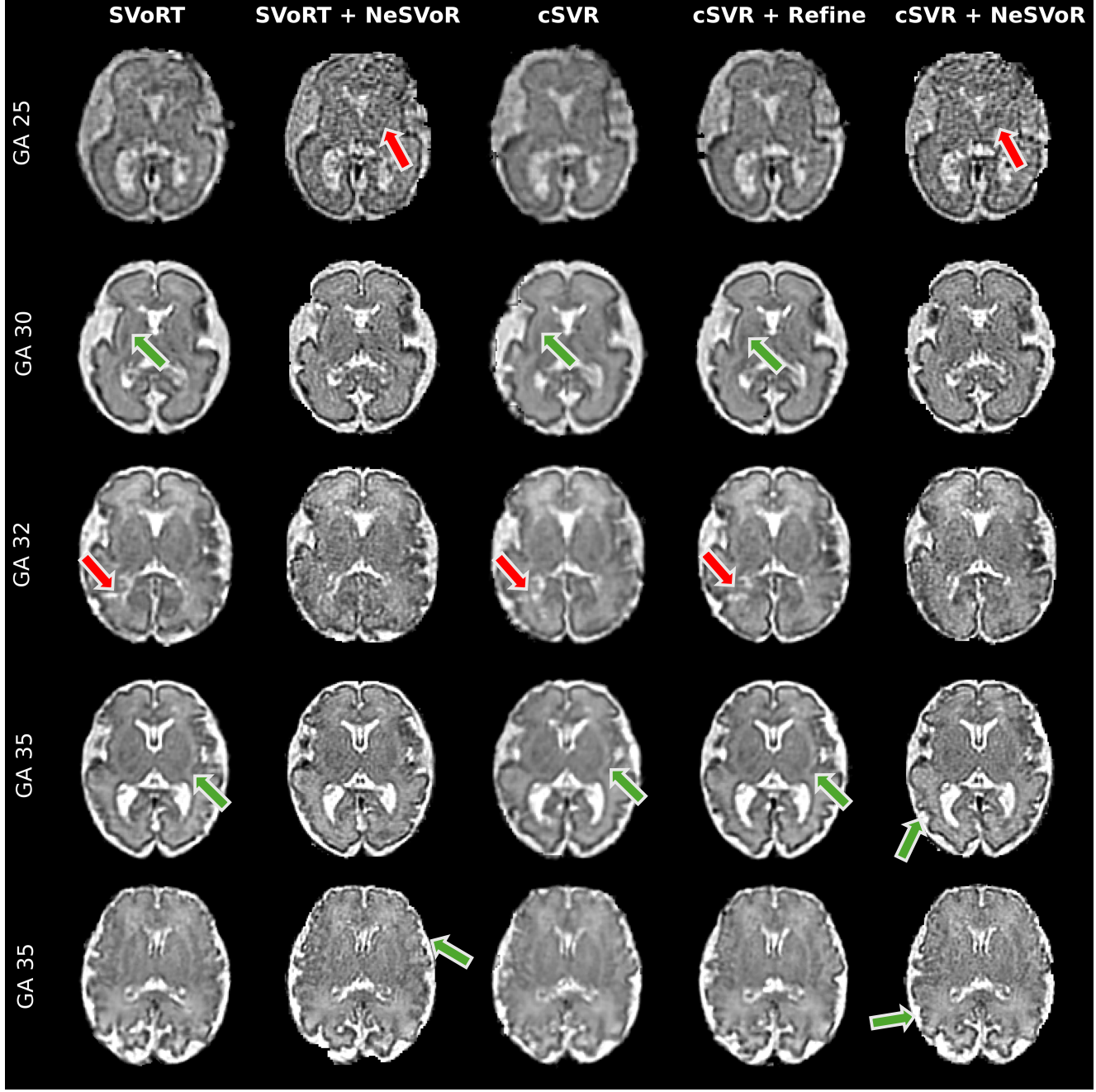


Figure 3: Clinical Evaluation. Reconstructions for clinical subjects (GA 20–35 weeks) for all methods: SVoRT, SVoRT + NeSVoR, cSVR, cSVR + Refine, cSVR + NeSVoR. Our proposed fast method, cSVR + Refine, achieves high-quality reconstructions comparable to state of the art, with high grey and white matter contrast (green arrows). Our method as well as SVoRT struggles in cases of image corruption as seen by the red arrows, where the reconstructions fail to exclude noisy areas of a slice.

continues to refine the slice poses while alternating with volume reconstruction; (3) cSVR+NeSVoR provides the slice poses estimated by the network as an initialization for NeSVoR, the state of the art method based on an implicit neural representation (INR) of the resulting volume [29]. We also compare the performance of the cSVR variants

with two baseline methods: a transformer-based approach SVoRT [28] and SVoRT+NeSVoR method that uses the output of SVoRT as an initialization for NeSVoR. SVoRT was trained on FeTA dataset [16] and shares the same validation set as our method.

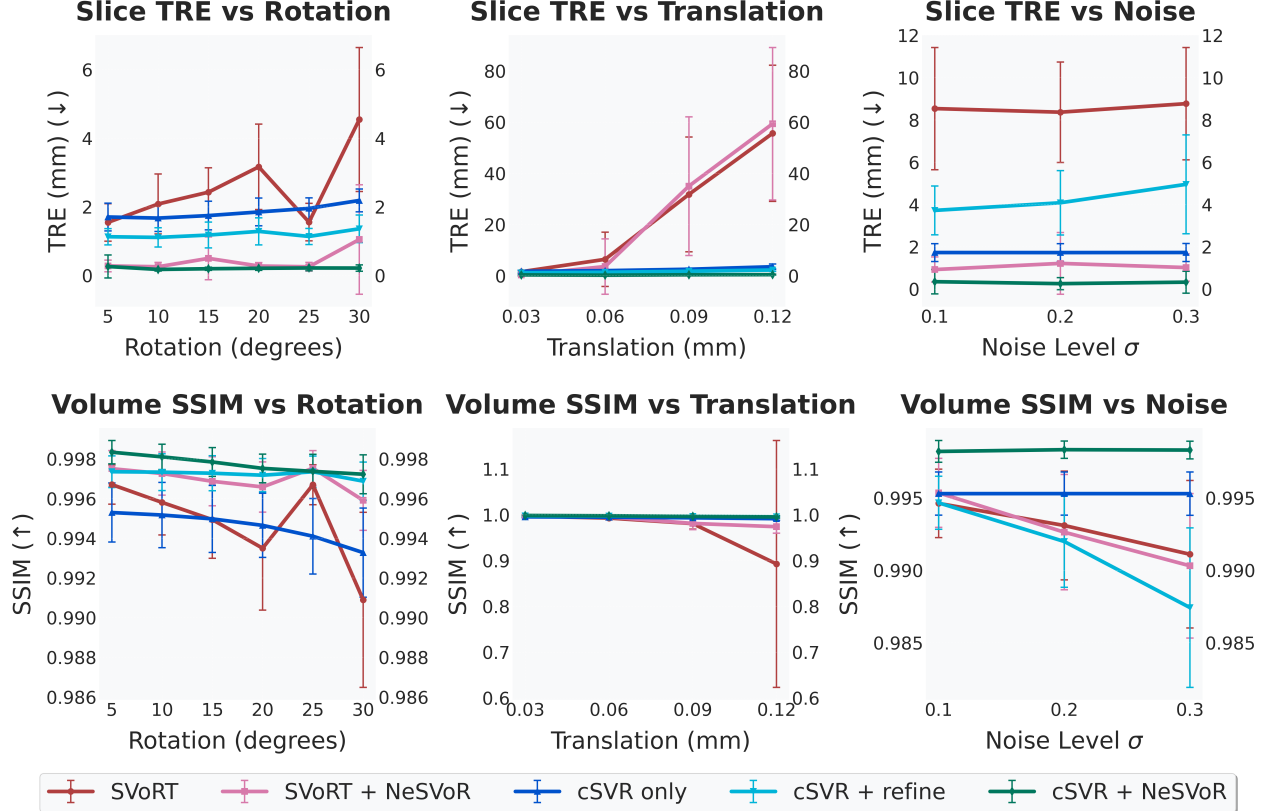


Figure 4: Performance evaluation and sensitivity analysis. Robustness across methods to input stack perturbations (translation, rotation, noise), evaluated via registration accuracy (top) and reconstruction quality (bottom). Our method, cSVR + refine, is robust across high levels of translation and rotation and our method coupled with NeSVoR reconstruction achieves the best overall performance.

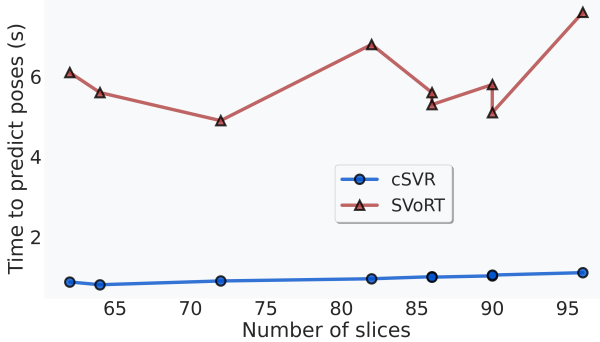


Figure 5: Inference Time of Registration Methods Time to predict slice poses on clinical subjects of varying input sizes, comparing SVoRT vs cSVR.

Evaluation on Synthetic Data. On the synthetic data, where ground truth is available, we quantify the accuracy of the pose prediction using the maximum total registration error (TRE) and volume reconstruction quality using structural similarity index measure (SSIM) [25] between the reconstructed and the ground truth volumes. For estimated

Table 2: Ablation Study. Effect of loss function and slice pose initialization on clinical data.

Slice poses initialized	Multi-layer loss applied	SSIM	NCC	PSNR
✗	✓	0.93	0.10	32.63
✓	✗	0.966	0.13	36.95
✓	✓	0.966	0.13	37.00

and ground-truth displacement fields \hat{f} and f , respectively, we define

$$\text{TRE}(\hat{f}; f) = \max_p \left\| \hat{f}(p) - f(p) \right\|_2 \quad (10)$$

which captures the point of maximum distance between the predicted pixel location and the ground truth location. Prior to computing the TRE, the output volume is registered to the ground-truth volume using ANTS [3] to mitigate the effect of global shifts in reconstruction. Although most previous work report only volume consistency scores, TRE is

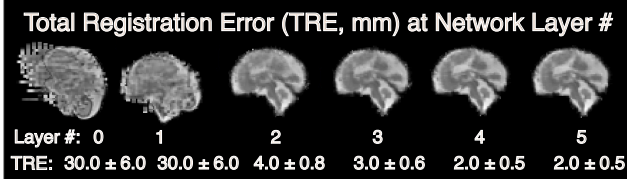


Figure 6: Pose estimation in different layers of the network. Network gradually estimates pose, with bulk of pose being predicted correctly in the first two layers.

an important measure to distinguish between the registration performance of a given method and its reconstruction performance. Notably, TRE scores for smaller slices, where only part of the brain is visible, are higher as these regions are harder to register. To mitigate this, we report median maximum TRE per slice stacks for the sensitivity analysis.

To capture high variability of motion in clinical practice, we evaluate our method on a range of motion settings, varying the possible range of sampled rotations and translations separately for 12 subjects. We also evaluate the methods’ ability to mitigate noise in the reconstruction by varying the noise level in the synthetic data.

Evaluation on Clinical Data. For clinical data, we evaluate the consistency between the estimated and acquired slices using mean SSIM, PSNR, and NCC (Table 1). We run all evaluations using an NVIDIA A6000 GPU.

5.1. Results

Synthetic data. We evaluate all methods for varying degree of corruptions, specifically varying rotations, translations, and image noise (Fig 4). Overall, cSVR is robust to large rotations, translations, and noise. Adding the refinement steps, cSVR + Refine, significantly boosts performance across all levels of rotations and translations. However, cSVR + Refine hurts performance in the case of high image noise. This is potentially explained as the refinement step is driven by slice consistency which is corrupted by noise. When our method is combined with INR reconstruction (NeSVoR) it achieves the most robust results of all methods. SVoRT struggles with high levels of rotation and translation. For rotation, NeSVoR is able to compensate, but for large translations the INR is not able to refine the pose adequately.

Clinical Data. In the clinical cases, we observe that our method performs similarly to the baseline methods, (Table 1). The SSIM, PSNR, and NCC are all close for all models, with our method being generally being the second best. NeSVoR is prone to slight intensity shifts that contribute to the lowest similarity metrics of the three despite visually high-quality reconstructions (Fig 3). Our method shows good contrast of grey matter and white matter, Fig.

(3 row 4). We observe NeSVoR + SVoRT produce sharp reconstructions, as can be seen by the fine detail in the cortex in the last row. However NeSVoR is also prone to make noisy reconstructions with a speckle-like pattern, as seen in the first row. An example of the problem of using only self-consistency metrics can be seen in the third subject (GA 32w) where a noisy slice contributes a bright spot on the left side of the brain. While all gradient-descent methods reconstruct this artifact, NeSVoR successfully suppresses it.

Ablations Studies. We evaluate the quality of the slice pose estimates for different layers of the network as seen in Fig. 6 and find the network gradually refines the pose, with large deformations occurring in the early layers. We empirically evaluate the runtime of the algorithms and validate that our method scales linearly with the input slice count while SVoRT (transformer-based) scales (roughly) quadratically (Fig. 5).

To test whether our parametrization of slice poses in (8) is necessary for network learning, we initialize all slices with only their slice index position by setting all rotations matrices R_n to identity, and train the network. In Table 2 we show the network has very poor performance in this case. We also evaluate the effect of using a multi-layer loss and see only a small improvement in PSNR.

6. Discussion

Limitations. Although our method could be used on multiple stacks, we only evaluated reconstructions based on 3 stack input. Our method requires pre-processing steps that could be integrated into the network such as standardizing slice ordering and orientations. We compared our method to state of the art SVR methods (SVoRT + NeSVoR), but additional insights could be gleaned by comparing with concurrent work [4, 26, 27] once the code has been made public.

Future work. We plan to extend this framework to non-rigid SVR applications such as placental MRI. We also plan to train the network to learn how to refine the poses and use a cascading scheme to do convolutional-based refinement.

7. Conclusions

We demonstrate a fast convolutional multi-stack SVR approach that is 40 times faster than the state of the art methods that produces comparable quality reconstructions. We propose a slice parameterization, loss function, and a robust reconstruction approach that enables this architecture to be generalized to other SVR applications.

Acknowledgments. This work is supported by NSF GRFP, NIH R01EB032708, R01HD114338, R01EB036945, K99AG081493 and R00AG081493, and the MIT CSAIL-Wistron Program.

References

[1] Michael Aertsen. The role of fetal brain magnetic resonance imaging in current fetal medicine. *J. Belg. Soc. Radiol.*, 106(1):130, 2022. 1

[2] K. S. Arun, T. S. Huang, and S. D. Blostein. Least-squares fitting of two 3-d point sets. *IEEE Transactions on Pattern Analysis and Machine Intelligence*, PAMI-9(5):698–700, 1987. 5

[3] Brian Avants, Nicholas J Tustison, and Gang Song. Advanced normalization tools: V1.0. *Insight J.*, 2009. 7

[4] Maik Dannecker, Thomas Sanchez, Meritxell Bach Cuadra, Özgün Turgut, Anthony N. Price, Lucilio Cordero-Grande, Vanessa Kyriakopoulou, Joseph V. Hajnal, and Daniel Rueckert. Meta-learning slice-to-volume reconstruction in fetal brain mri using implicit neural representations, 2025. 2, 3, 8

[5] Michael Ebner, Guotai Wang, Wenqi Li, Michael Aertsen, Premal A. Patel, Rosalind Aughwane, Andrew Melbourne, Tom Doel, Steven Dymarkowski, Paolo De Coppi, Anna L. David, Jan Deprest, Sébastien Ourselin, and Tom Vercauteren. An automated framework for localization, segmentation and super-resolution reconstruction of fetal brain mri. *NeuroImage*, 206:116324, 2020. 2

[6] Michael Ebner, Guotai Wang, Wenqi Li, Michael Aertsen, Premal A Patel, Rosalind Aughwane, Andrew Melbourne, Tom Doel, Steven Dymarkowski, Paolo De Coppi, et al. An automated framework for localization, segmentation and super-resolution reconstruction of fetal brain MRI. *NeuroImage*, 206:116324, 2020.

[7] Ali Gholipour, Judy A Estroff, and Simon K Warfield. Robust super-resolution volume reconstruction from slice acquisitions: application to fetal brain MRI. *IEEE transactions on medical imaging*, 29(10):1739–1758, 2010. 2

[8] Ali Gholipour, Caitlin K Rollins, Clemente Velasco-Annis, Abdelhakim Ouaalam, Alireza Akhondi-Asl, Onur Afacan, Cynthia M Ortinau, Sean Clancy, Catherine Limperopoulos, Edward Yang, Judy A Estroff, and Simon K Warfield. A normative spatiotemporal MRI atlas of the fetal brain for automatic segmentation and analysis of early brain growth. *Sci. Rep.*, 7(1):476, 2017. 5

[9] Paul D Griffiths, Michael Bradburn, Michael J Campbell, Cindy L Cooper, Ruth Graham, Deborah Jarvis, Mark D Kilby, Gerald Mason, Cara Mooney, Stephen C Robson, Allan Wailoo, and MERIDIAN collaborative group. Use of MRI in the diagnosis of fetal brain abnormalities in utero (MERIDIAN): a multi-centre, prospective cohort study. *Lancet*, 389(10068):538–546, 2017. 1

[10] Benjamin Hou, Bishesh Khanal, Amir Alansary, Steven McDonagh, Alice Davidson, Mary Rutherford, Jo V. Hajnal, Daniel Rueckert, Ben Glocker, and Bernhard Kainz. 3d reconstruction in canonical co-ordinate space from arbitrarily oriented 2d images, 2018. 2

[11] Shuzhou Jiang, Hui Xue, Alan Glover, Mary Rutherford, Daniel Rueckert, and Joseph V Hajnal. MRI of moving subjects using multislice snapshot images with volume reconstruction (SVR): application to fetal, neonatal, and adult brain studies. *IEEE transactions on medical imaging*, 26(7):967–980, 2007. 2, 3

[12] Bernhard Kainz, Markus Steinberger, Wolfgang Wein, Maria Kuklisova-Murgasova, Christina Malamateniou, Kevin Keraudren, Thomas Torsney-Weir, Mary Rutherford, Paul Aljabar, Joseph V Hajnal, et al. Fast volume reconstruction from motion corrupted stacks of 2d slices. *IEEE transactions on medical imaging*, 34(9):1901–1913, 2015. 2

[13] Uday Krishnamurthy, Jaladhar Neelavalli, Swati Mody, Lami Yeo, Pavan K Jella, Sheena Saleem, Steven J Korzeniewski, Maria D Cabrera, Shadi Ehterami, Ray O Bahado-Singh, Yashwanth Katkuri, Ewart M Haacke, Edgar Hernandez-Andrade, Sonia S Hassan, and Roberto Romero. MR imaging of the fetal brain at 1.5T and 3.0T field strengths: comparing specific absorption rate (SAR) and image quality. *J. Perinat. Med.*, 43(2):209–220, 2015. 1

[14] Maria Kuklisova-Murgasova, Gerardine Quaghebeur, Mary A. Rutherford, Joseph V. Hajnal, and Julia A. Schnabel. Reconstruction of fetal brain mri with intensity matching and complete outlier removal. *Medical Image Analysis*, 16(8):1550–1564, 2012. 2, 5

[15] Lucia Manganaro, Silvia Capuani, Marco Gennarini, Valentina Miceli, Roberta Ninkova, Ilaria Balba, Nicola Galea, Angelica Cupertino, Alessandra Maiuro, Giada Ercolani, and Carlo Catalano. Fetal mri: what's new? a short review. *European Radiology Experimental*, 7(1):41, 2023. 1

[16] Kelly Payette, Priscille de Dumast, Hamza Kebiri, Ivan Ezhov, Johannes Paetzold, Suprosanna Shit, Asim Iqbal, Romesa Khan, Raimund Kottke, Patrice Grehten, Hui Ji, Levente Lanczi, Marianna Nagy, Beres Monika, Thi Nguyen, Giancarlo Natalucci, Theofanis Karayannis, Bjoern Menze, Meritxell Bach Cuadra, and András Jakab. An automatic multi-tissue human fetal brain segmentation benchmark using the fetal tissue annotation dataset. *Scientific Data*, 8, 2021. 5, 6

[17] Yuchen Pei, Lisheng Wang, Fenqiang Zhao, Tao Zhong, Lufan Liao, Dinggang Shen, and Gang Li. Anatomy-guided convolutional neural network for motion correction in fetal brain mri. In *Machine*

Learning in Medical Imaging, pages 384–393, Cham, 2020. Springer International Publishing. 2

[18] Daniela Prayer, Peter Christian Brugger, and Lucas Prayer. Fetal MRI: techniques and protocols. *Pediatr. Radiol.*, 34(9):685–693, 2004. 1

[19] Marta B. M. Ranzini, Lucas Fidon, Sébastien Ourselin, Marc Modat, and Tom Vercauteren. Monai-aifbs: Monai-based fetal brain mri deep learning segmentation, 2021. 5

[20] Olaf Ronneberger, Philipp Fischer, and Thomas Brox. U-net: Convolutional networks for biomedical image segmentation. In *International Conference on Medical image computing and computer-assisted intervention*, pages 234–241. Springer, 2015. 3

[21] François Rousseau, Orhan A Glenn, Betina Iordanova, Cynthia Rodriguez-Carranza, Daniel B Vigneron, A James Barkovich, and Colin Studholme. Registration-based approach for reconstruction of high-resolution in utero fetal mr brain images. *Academic Radiology*, 13(9):1072–1081, 2006. 2, 3

[22] Seyed Sadegh Mohseni Salehi, Shadab Khan, Deniz Erdogmus, and Ali Gholipour. Real-time deep pose estimation with geodesic loss for image-to-template rigid registration, 2018. 2

[23] Sébastien Tourbier, Xavier Bresson, Patric Hagmann, Jean-Philippe Thiran, Reto Meuli, and Meritxell Bach Cuadra. An efficient total variation algorithm for super-resolution in fetal brain MRI with adaptive regularization. *NeuroImage*, 118:584–597, 2015. 2

[24] Alena U. Uus, Alexia Egloff Collado, Thomas A. Roberts, Joseph V. Hajnal, Mary A. Rutherford, and Maria Deprez. Retrospective motion correction in foetal mri for clinical applications: existing methods, applications and integration into clinical practice. *British Journal of Radiology*, 96(1147):20220071, 2022. 2

[25] Zhou Wang, Alan Conrad Bovik, Hamid Rahim Sheikh, and Eero P Simoncelli. Image quality assessment: from error visibility to structural similarity. *IEEE Trans. Image Process.*, 13(4):600–612, 2004. 7

[26] Jiangjie Wu, Lixuan Chen, Zhenghao Li, Xin Li, Tao-tao Sun, Lihui Wang, Rongpin Wang, Hongjiang Wei, and Yuyao Zhang. 3D isotropic high-resolution fetal brain MRI reconstruction from motion corrupted thick data based on physical-informed unsupervised learning. *IEEE J. Biomed. Health Inform.*, PP(99):1–14, 2025. 3, 8

[27] Jiangjie Wu, Hongjiang Wei, and Yuyao Zhang. Svr-mamba: Slice-to-volume reconstruction from multiple mri stacks with slice sequence guided mamba. *Proceedings of the AAAI Conference on Artificial Intelligence*, 39(8):8404–8412, 2025. 2, 8

[28] Junshen Xu, Daniel Moyer, P. Ellen Grant, Polina Golland, Juan Eugenio Iglesias, and Elfar Adalsteinsson. Svort: Iterative transformer for slice-to-volume registration in fetal brain mri. In *Medical Image Computing and Computer Assisted Intervention – MICCAI 2022*, pages 3–13, Cham, 2022. Springer Nature Switzerland. 2, 3, 5, 6, 11

[29] Junshen Xu, Daniel Moyer, Borjan Gagoski, Juan Eugenio Iglesias, P. Ellen Grant, Polina Golland, and Elfar Adalsteinsson. Nesvor: Implicit neural representation for slice-to-volume reconstruction in mri. *IEEE Transactions on Medical Imaging*, 42(6):1707–1719, 2023. 2, 3, 6, 11

[30] Sean I. Young, Yaël Balbastre, Bruce Fischl, Polina Golland, and Juan Eugenio Iglesias. Fully convolutional slice-to-volume reconstruction for single-stack mri, 2024. 2, 3, 5

Fast Multi-Stack Slice-to-Volume Reconstruction via Multi-Scale Unrolled Optimization

Supplementary Material

In this supplement, we provide additional details of methods described in the paper, additional ablations, and visual results.

A. Implementation Details

Network architecture. Our specialized U-net has 10 layers, five in the encoder and five in the decoder. Each layer consists of 4 convolutions with 2D kernel of size (1,3,3) in the encoder and 3D kernel in the decoder (2,3,3). In the decoder, the volume recon and slice prediction are forward operators while the field update is a convolutional layer.

B. Model-based reconstruction

We use an implementation from the NeSVoR package [29] for model-based reconstruction by calling the command `nesvor svr` with slices that are initialized with the network’s predicted pose. We use the options `--no-global-exclusion`, `--n-iter 5`, and `--n-iter-rec 3`. Disabling global exclusions avoids large holes in the reconstruction caused by many slices being excluded. We find that increasing the number of outer iterations (`n-iter`) from 3 to 5 improves results and thus fewer inner loops (`n-iter-rec`) are needed. After reconstruction, we rescale the volume by the average of the slice scaling factors to avoid global shifts in intensity. We disable the pose refinement step in the case of using cSVR alone and enable it to perform cSVR + Refine.

C. Baselines

SVoRT Baseline. We use the latest version of the SVoRT package (v2) [28] provided in the NeSVoR library by calling the command `nesvor svr` with the motion-corrupted stacks. We use the options `--no-global-exclusion`, `--n-iter 5`, and `--n-iter-rec 3` to ensure consistency with the model-based reconstruction. We similarly rescale the slices to avoid global shifts in the reconstructed volume.

NeSVoR. We use the original reference implementation

provided in the NeSVoR library by calling the command `nesvor reconstruct`. We additionally disable the `output-mean-intensity` functionality to ensure the volumes are reconstructed in the same range as the input slices.

D. Model Scale

We downscale each layer’s features by a factor of 2,4,8 and compute the model’s performance on the clinical test cases. This corresponds to the number of parameters in Table 3. The largest gain is from scaling the model to over 100 M parameters. At very small model sizes, there is large variations in performance across models.

Table 3: Ablation Study. Effect of total number of parameters

Model size	SSIM (↑)	NCC (↑)	PSNR (↑)
10 M	0.961	0.126	36.2
14 M	0.947	0.113	34.7
165 M	0.966	0.132	36.9
660 M (cSVR)	0.966	0.132	37.0

E. Additional Results

We compare reconstructions from synthetic data under severe rotation, translation, and noise corruption across the different methods (Fig. 7). Our model with refinement (cSVR + Refine) reconstructs coherent brains in all three cases. The most notable difference between methods in the case of large translation. It is important to note that the INR-based method (NeSVoR) fails to reconstruct the brain areas in places of poor coverage and instead creates black spots. We also provide coronal and sagittal views of the clinical subjects provided in the main paper as well as 4 other subjects of the 9 used for evaluation in the paper (Fig. 3). Our method performs comparably to state of the art with significant time improvements.

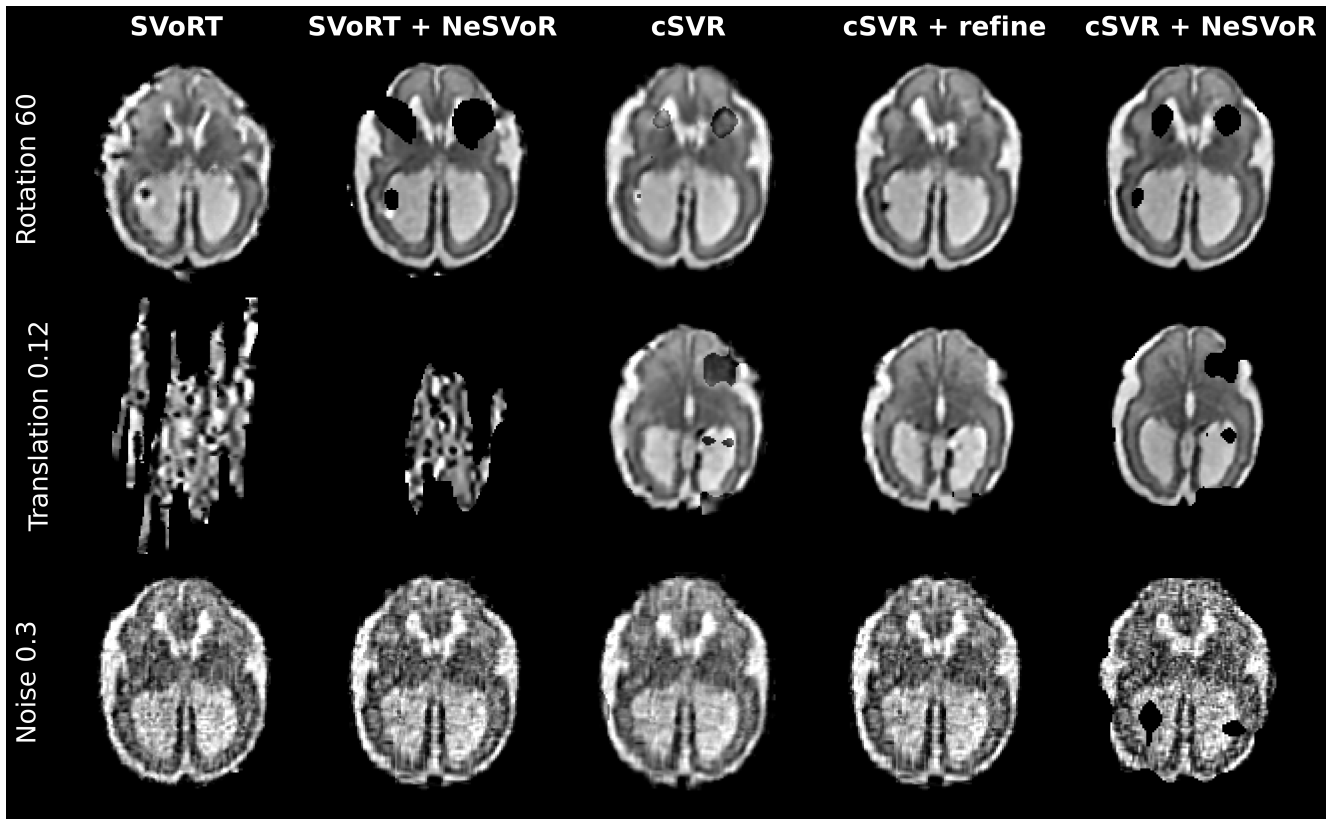


Figure 7: Synthetic Evaluation. Reconstructions from one synthetic subject with high rotation, translation, and noise. Our model with refinement (cSVR + Refine) performs well in all three corruption scenarios, with the most notable difference in the case of translation. INR based methods create black areas in places of poor coverage.

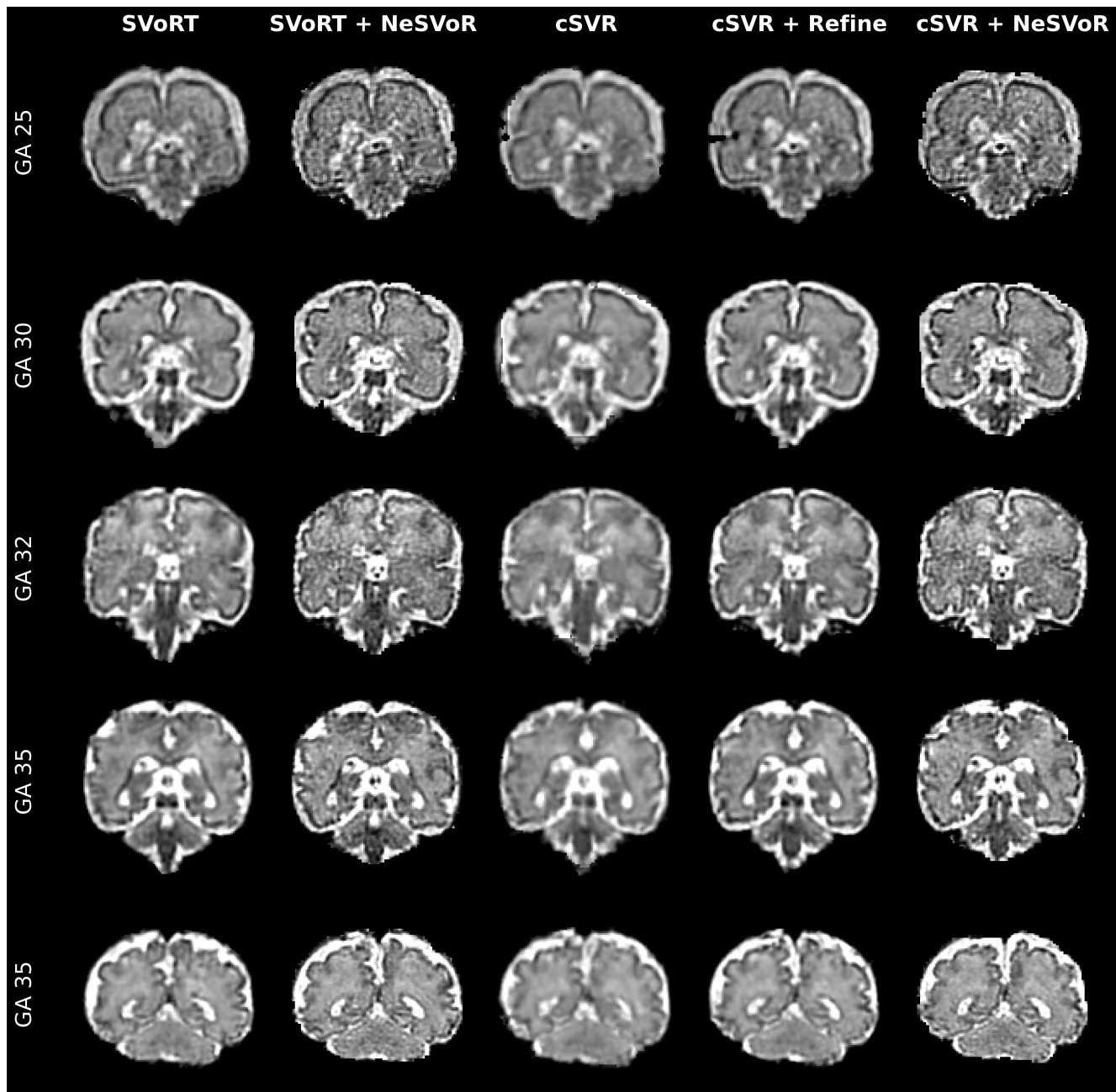


Figure 8: Clinical Evaluation Coronal View. Reconstructions for 5 clinical subjects (GA 20–35 weeks) for all methods: SVoRT, SVoRT + NeSVoR, cSVR, cSVR + Refine, cSVR + NeSVoR.

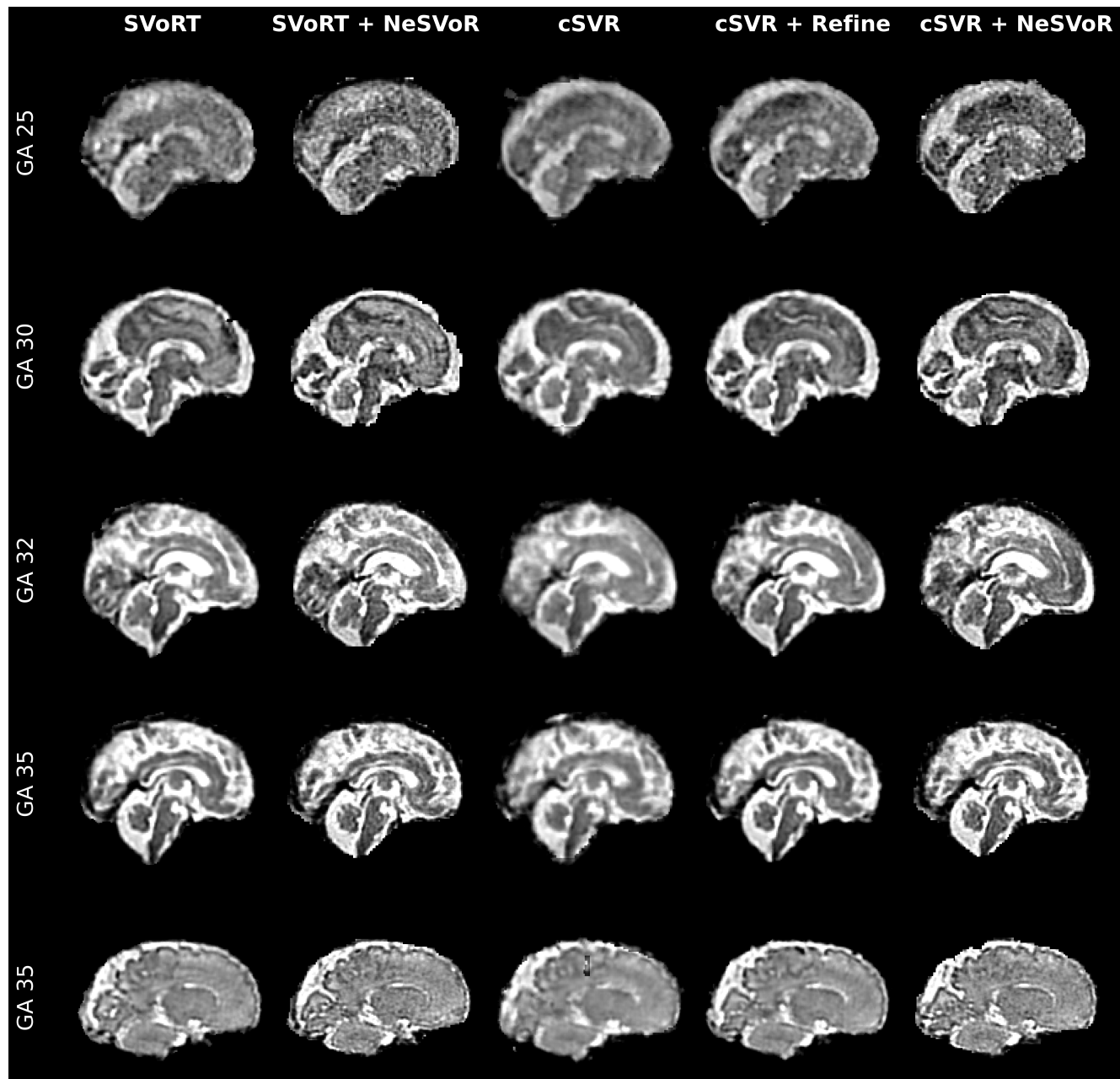


Figure 9: Clinical Evaluation Sagittal View. Reconstructions for 5 clinical subjects (GA 20–35 weeks) for all methods: SVoRT, SVoRT + NeSVoR, cSVR, cSVR + Refine, cSVR + NeSVoR.

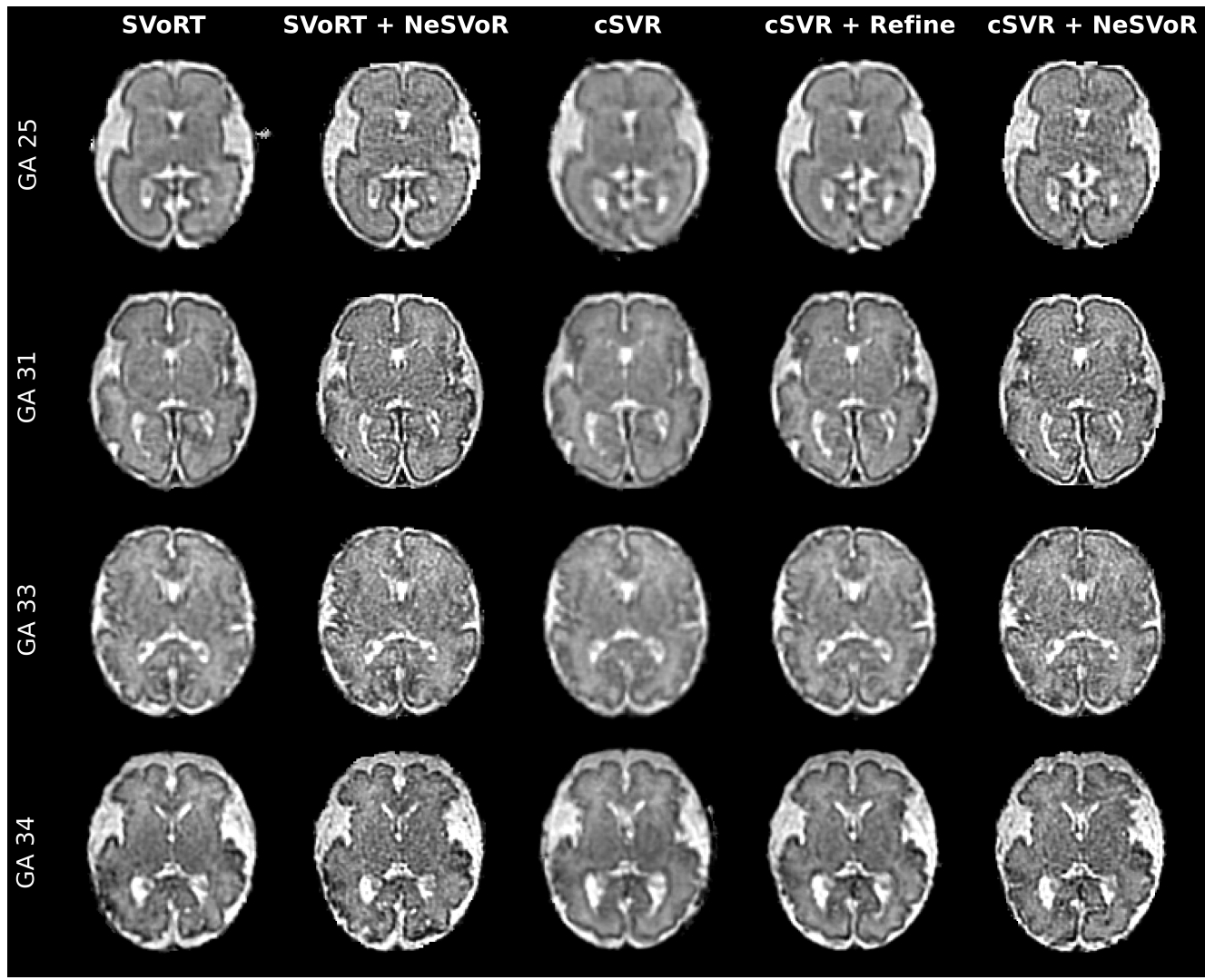


Figure 10: Clinical Evaluation Axial View. Reconstructions on 4 other clinical subjects (GA 20–35 weeks) for all methods: SVoRT, SVoRT + NeSVoR, cSVR, cSVR + Refine, cSVR + NeSVoR.

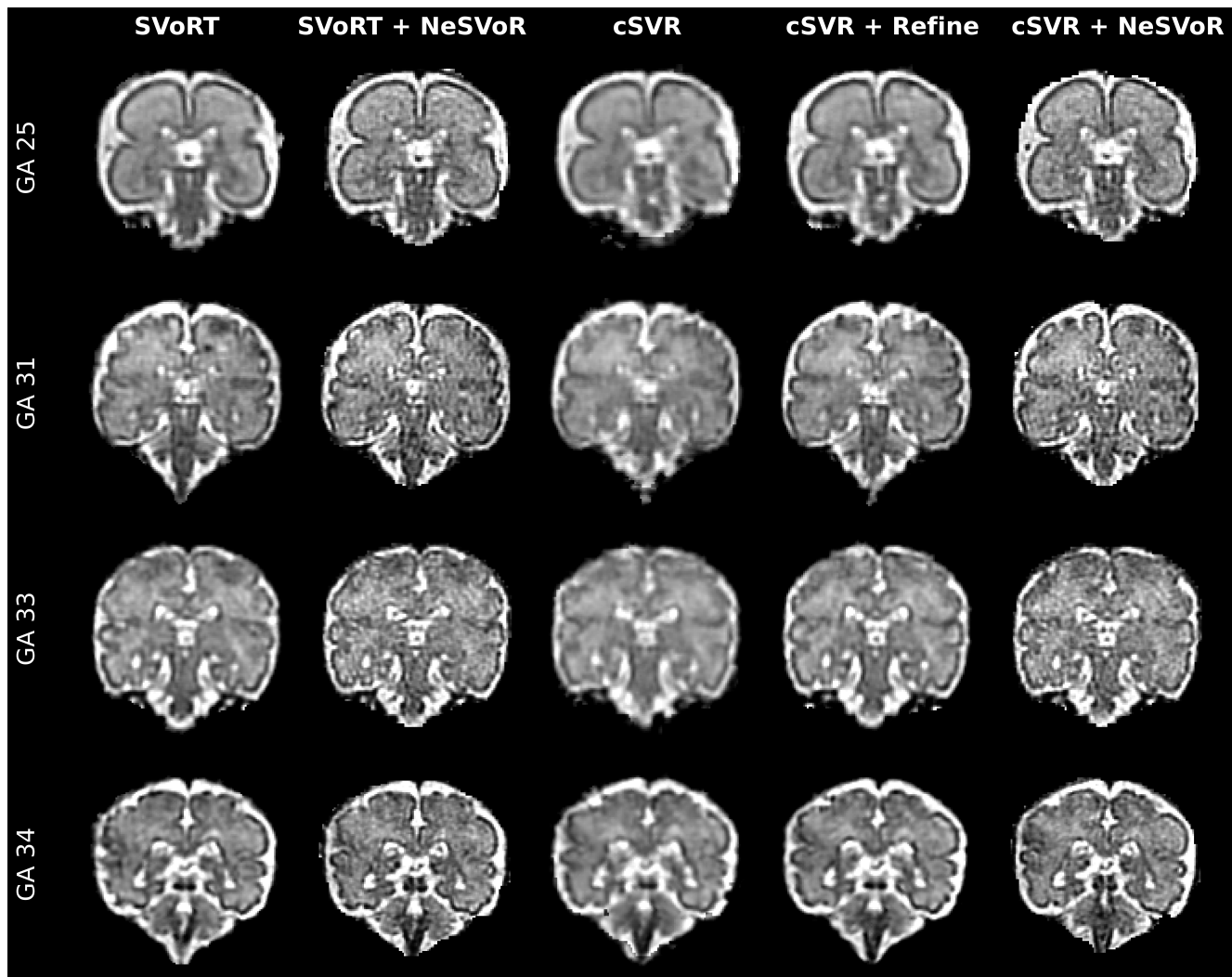


Figure 11: Clinical Evaluation Coronal View. Reconstructions on 4 other clinical subjects (GA 20–35 weeks) for all methods: SVoRT, SVoRT + NeSVoR, cSVR, cSVR + Refine, cSVR + NeSVoR.

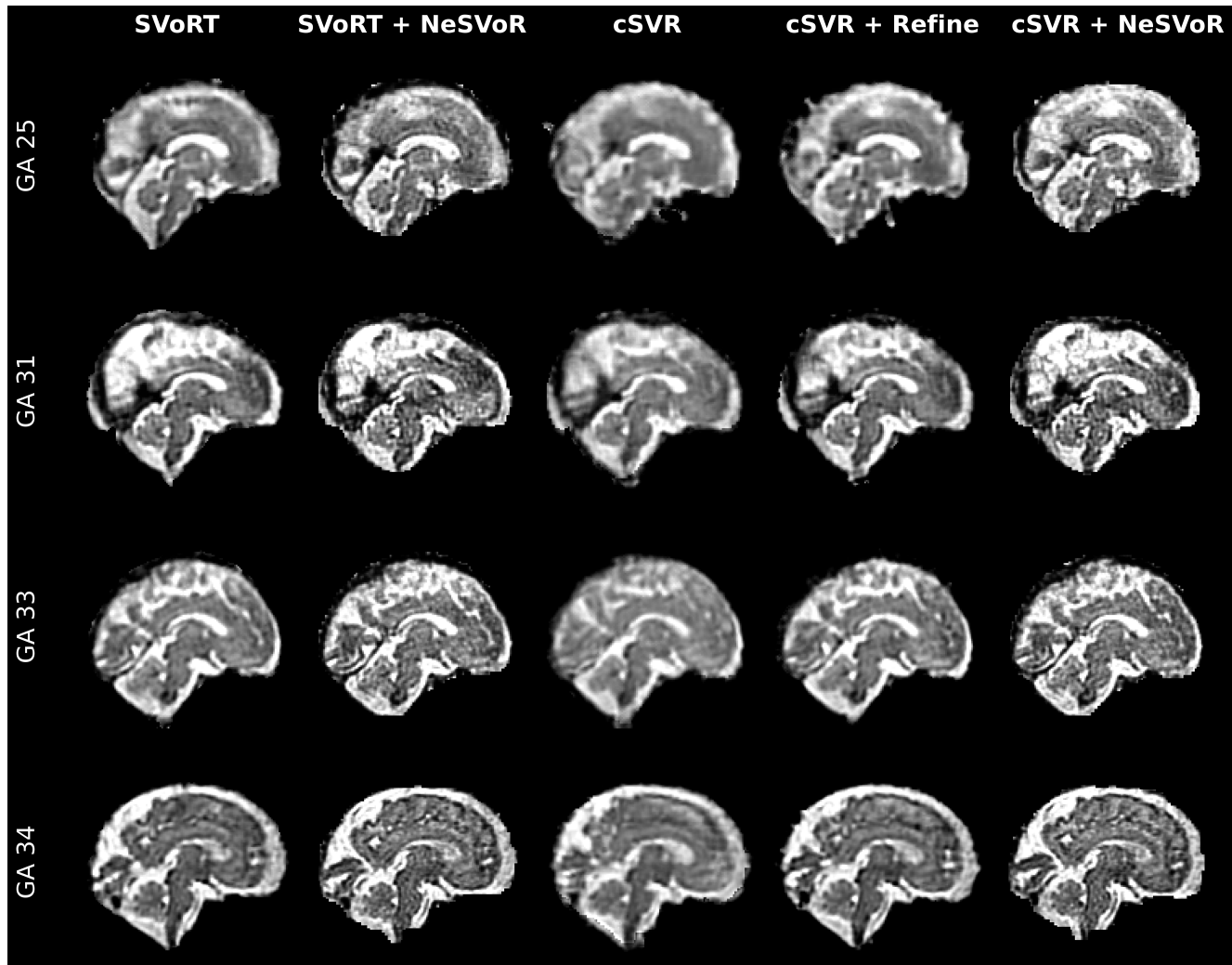


Figure 12: Clinical Evaluation Sagittal View. Reconstructions on 4 other clinical subjects (GA 20–35 weeks) for all methods: SVoRT, SVoRT + NeSVoR, cSVR, cSVR + Refine, cSVR + NeSVoR.